Thickness-dependent structural characteristics for a sputtering-deposited chromium monolayer and Cr/C and Cr/Sc multilayers

Hui Jiang,[a] Hua Wang,[a]* Jingtao Zhu,[b]* Chaofan Xue,[a] Jiayi Zhang,[b] Naxi Tian[a] and Aiguo Li[a]

[a]Shanghai Synchrotron Radiation Facility, Shanghai Institute of Applied Physics, Chinese Academy of Sciences, 239 Zhangheng Road, Pudong District, Shanghai 201204, People's Republic of China, and [b]MOE Key Laboratory of Advanced Micro-Structured Materials, School of Physics Science and Engineering, Tongji University, Shanghai 200092, People's Republic of China. *Correspondence e-mail: wanghua@sinap.ac.cn, jtzhu@tongji.edu.cn

The interior structure, morphology and ligand surrounding of a sputtering-deposited chromium monolayer and Cr/C and Cr/Sc multilayers are determined by various hard X-ray techniques in order to reveal the growth characteristics of Cr-based thin films. A Cr monolayer presents a three-stage growth mode with sudden changes occurring at a layer thickness of ~2 nm and beyond 6 nm. Cr-based multilayers are proven to have denser structures due to interfacial diffusion and layer growth mode. Cr/C and Cr/Sc multilayers have different interfacial widths resulting from asymmetry, degree of crystallinity and thermal stability. Cr/Sc multilayers present similar ligand surroundings to Cr foil, whereas Cr/C multilayers are similar to Cr monolayers. The aim of this study is to help understand the structural evolution regulation *versus* layer thickness and to improve the deposition technology of Cr-based thin films, in particular for obtaining stable Cr-based multilayers with ultra-short periods.

1. Introduction

Multilayers with short (several nanometres) or ultra-short (less than 2.5 nm) periods have particular applications in the soft X-ray to X-ray regimes. One of the most significant applications is water-window (~2.3–4.4 nm) (Stollberg *et al.*, 2006) and near-water-window (4.4–6.7 nm) (Deng *et al.*, 2009) soft X-ray microscopy. The periodic thickness of the multilayer satisfies the interference conditions for obtaining high reflectivity near normal incidence. Regarding grazing-incidence monochromators, the periodic thickness of the multilayer needs to be controlled such that it is short enough to enable a high penetration depth (Andreev *et al.*, 2003). Interfacial roughness is considered to be more important than chemical stability and the difference of optical constants in obtaining high reflectivity with short periods (Jergel *et al.*, 2008). Amorphous layers are preferred to polycrystalline in order to obtain smooth interfaces (Jergel *et al.*, 2008). For lateral gradient multilayers for Kirkpatrick–Baez focusing mirrors (Hignette *et al.*, 2007) and depth gradient multilayers for Laue lenses (Yan *et al.*, 2007), their thinnest layer determines the spatial resolution of focusing. In order to satisfy the extreme requirements of both the interface quality and the thin-film density, the deposition and characterization of such thin layers are always challenging.

Cr-based multilayers are one of the most attractive material pairs for short periods for satisfying different energy ranges. In the hard X-ray regime, Cr is the best material for energies below the Cr *K*-edge (~6 keV) and an important material for
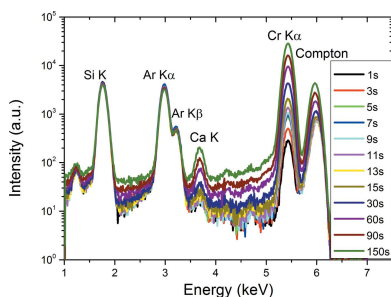
energies higher than 20 keV. In the water window regime, Cr has suitable optical constants as a scattering layer and sharp interfaces to combine with carbon (Deng *et al.*, 2009), scandium (Stollberg *et al.*, 2006; Majkova *et al.*, 2006; Gullikson *et al.*, 2006), titanium (Gullikson *et al.*, 2006) and vanadium (Gullikson *et al.*, 2006; Huang *et al.*, 2016), *etc.* in order to obtain high reflectivity. In the soft X-ray and extreme-ultraviolet (EUV) regimes, Cr/C multilayers are typical polarization elements at the quasi-Brewster angle (Niibe *et al.*, 2004; Wen *et al.*, 2015). Aperiodic chirped Cr/Sc multilayers were reported for attosecond pulse shaping in the water window range (Guggenmos *et al.*, 2013). Fe/Cr (Miyanaga *et al.*, 2014), Co/Cr (Ramakrishna *et al.*, 1987) and Gd/Cr (Gadioli *et al.*, 2013) multilayers also display good magnetic performances.

Deposition technologies have been investigated in order to decrease the loss of reflectivity. Incorporation of nitrogen (Ghafoor *et al.*, 2008), ion assist (Birch *et al.*, 2003), B_4C co-sputtering (Ghafoor *et al.*, 2017), inserting barrier layers (Huang *et al.*, 2016; Hatano *et al.*, 2017), *etc.* during the deposition were shown to improve the interfaces, thermal stability and stress in Cr-based multilayers. Accurate structural characterizations were carried out to gain further knowledge about the interface characteristics in Cr/C or Cr/B_4C multi-layers by grazing-incidence X-ray reflectometry (Alnaimi *et al.*, 2016; Burcklen *et al.*, 2016), transmission electron microscopy (TEM) (Jiang *et al.*, 2011; Burcklen *et al.*, 2016) and Raman spectrometry (Tu *et al.*, 2014), *etc.* Cr/Sc multilayers were also investigated by TEM and X-ray scattering to study their thermal stability (Majkova *et al.*, 2006). A combined analysis of different experimental methods was demonstrated to robustly determine the properties of ultra-thin Cr/Sc multilayers (Haase *et al.*, 2016).

The previously mentioned studies mainly focus on the relationship between multilayer microstructure and optical performance. Some parameters were optimized in the pursuit of a higher reflectance performance. However, for Cr-based multilayers there have been few studies on their initial growth and structure evolution *versus* layer thickness. Different layer thicknesses may result in very different structural characteristics. Studying the thickness dependence enables the applications of Cr-based multilayers to be more relevant and systematic. In this paper, we combine various measurement methods, such as grazing-incidence X-ray reflectometry (GIXRR), grazing-incidence X-ray diffraction (GIXRD), X-ray fluorescence spectroscopy (XRF), X-ray absorption near-edge structure (XANES) and atomic force microscopy (AFM), to investigate the structural evolution regulation of Cr monolayers and Cr/C and Cr/Sc multilayers *versus* the layer thickness, focusing particularly on the characteristics of the Cr layer in different short-period multilayers.

2. Experiments

2.1. Samples

Multilayer samples were deposited by direct-current magnetron sputtering on silicon wafers at room temperature.

All silicon wafers were polished and cleaned using the same methods and maintained a similar surface roughness. The base pressure was 1.0^{-4} Pa and the argon gas pressure was 0.13 Pa. The target-to-substrate distance for all targets was 80 mm. Samples S1–S12 were Cr monolayers with different deposition time t from 1 to 150 s; S13–S16 were Cr/C multilayers; S17–S20 were Cr/Sc multilayers and S21 was a Sc monolayer with a deposition time of 150 s. The power on the Cr, Sc and C targets was 60, 30 and 120 W, respectively. The bi-layer number for S13 and S17 is $N = 40$ and that of the other multilayer samples is $N = 20$. Larger periodic numbers were chosen for the thinnest samples S13 and S17 in order to obtain stronger interference and spectrum signals.

2.2. Experimental setup

The GIXRD data were obtained at the XRD beamline (BL14B1) (Yang *et al.*, 2015) of the Shanghai Synchrotron Radiation Facility (SSRF) using X-rays at an energy of 18 keV. The grazing-incidence angle was fixed at 0.5° and the detector was scanned over a wide angle range. During the annealing measurements, four multilayers with maximum thickness difference (S13, S16, S17 and S20) were placed into a chamber and the wafers were heated up from room temperature to ~600°C by a heating stage.

The XRF and XANES measurements were carried out at room temperature at the hard X-ray micro-focusing beamline (BL15U1) (Zhang *et al.*, 2015). The fluorescence signal in XRF measurements was collected by a silicon drift detector in 30 s at an energy of 6 keV. The fluorescence signal in XANES measurements was collected by scanning the energy around the Cr K-edge with a step size of 0.5 eV. The size of the beam spot during these measurements was ~3 µm × 3 µm.

The GIXRR curves were measured using a θ–2θ scan by an X-ray diffractometer at the energy of the Cu K_α line at room temperature. The surface morphology of Cr monolayers was measured by an NT-MDT atomic force microscope with different scanning ranges from 50 mm × 50 nm to 20 µm × 20 µm in a 256 × 256-pixel image.

3. Results and discussions

3.1. Structure and morphology characterizations

Theoretical GIXRR curves as a function of grazing-incidence angle for all samples can be calculated based on Parratt's recurrence formula (Parratt, 1954). The experimental data were fitted by theoretical data based on the least-squares method to obtain information on the layer thickness d, density ρ, roughness σ, *etc.* Fig. 1 shows the GIXRR curves and their fitted curves for Cr monolayers (S1–S12). The fluorescence spectra for these layers can be found in Fig. 2 for which the relative content of element Cr can be compared by calculating the integral intensities around the Cr K_α line. The integral intensity I is assumed to be proportional to the content of Cr due to the relatively low background signal. AFM was used to measure the surface morphology directly with different scanning ranges. The morphology of each AFM scan can be

Table 1
Structural parameters of Cr layers determined by GIXRR, AFM and XRF.

	t (s)	d (nm)	ρ (% bulk)	σ (nm) by GIXRR	σ (nm) by AFM	ζ (nm)	I (counts s^{-1}) by XRF
S1	1	0.6 ± 0.0	83.7 ± 3.1	0.99 ± 0.08	0.16 ± 0.03	349.1 ± 13.1	178.9 ± 5.8
S2	3	1.2 ± 0.0	70.0 ± 4.5	0.71 ± 0.07	0.15 ± 0.02	250.8 ± 11.0	311.4 ± 11.0
S3	5	1.9 ± 0.0	52.5 ± 3.0	0.57 ± 0.07	0.10 ± 0.02	222.6 ± 11.9	527.9 ± 17.1
S4	7	1.6 ± 0.0	58.2 ± 3.1	0.53 ± 0.06	0.13 ± 0.02	250.8 ± 12.5	572.7 ± 18.2
S5	9	1.9 ± 0.1	55.3 ± 3.7	0.44 ± 0.06	0.16 ± 0.03	228.4 ± 13.09	637.6 ± 20.3
S6	11	1.9 ± 0.0	63.1 ± 3.8	0.45 ± 0.06	0.15 ± 0.03	251.5 ± 12.6	809.9 ± 26.1
S7	13	2.2 ± 0.1	63.4 ± 4.0	0.62 ± 0.07	0.18 ± 0.03	335.8 ± 14.4	1185.8 ± 33.8
S8	15	2.1 ± 0.0	62.1 ± 3.8	0.49 ± 0.08	0.12 ± 0.02	254.3 ± 11.8	1247.8 ± 38.0
S9	30	3.6 ± 0.1	73.1 ± 4.0	0.49 ± 0.09	0.16 ± 0.03	214.5 ± 13.1	2564.6 ± 81.2
S10	60	6.1 ± 0.0	67.2 ± 3.8	0.55 ± 0.10	0.17 ± 0.03	303.6 ± 17.5	5725.4 ± 180.2
S11	90	9.2 ± 0.1	99.9 ± 3.1	0.95 ± 0.11	0.24 ± 0.04	162.9 ± 13.0	9655.8 ± 304.2
S12	150	14.7 ± 0.1	98.0 ± 3.5	1.07 ± 0.13	0.25 ± 0.08	161.9 ± 11.5	17156.6 ± 576.1

transformed into a one-dimensional power spectral density (PSD) curve in a specific spatial frequency range (Chkhalo *et al.*, 2014). By fitting these power spectral density curves simultaneously, the surface roughness σ and lateral correlation

Figure 1
GIXRR curves (black points) of Cr layers (S1–S12) with different deposition time and their fitted curves (red lines).

Figure 2
XRF spectra of Cr layers (S1–S12) with different deposition time measured at 6 keV. The Ar element signal was from the atmosphere and that of Ca was from impurities in the Cr targets.

length ζ can be determined (Yu *et al.*, 2008), where the lateral correlation length describes the layer growth correlation and relates to the grain size. Table 1 lists these structural parameters and comparisons between different methods are presented in Fig. 3.

The Cr content can also be estimated by the GIXRR method by the relation $C \propto \int \rho \, dz$, for a monolayer of depth z including a layer with constant density and a surface region where the density satisfies an error function. The Cr contents estimated by XRF and GIXRR are found to have a similar tendency. The content estimated by XRF gives a more linear profile and has lower content at the initial growth stage, as can be seen in Fig. 3. The reasons for the difference between the two methods are that (i) the beam sizes for the two measurements are different; (ii) the parameters of the layer thickness and density have a coupling relationship in the GIXRR fitting process, and (iii) the content calculated from GIXRR is influenced by surface oxidation and nitridation while XRF results come totally from the Cr signal. The surface roughnesses as a function of deposition time measured by the two methods have a similar trend but very different values. The roughnesses measured by GIXRR are at least three times greater than those measured by AFM. This phenomenon is
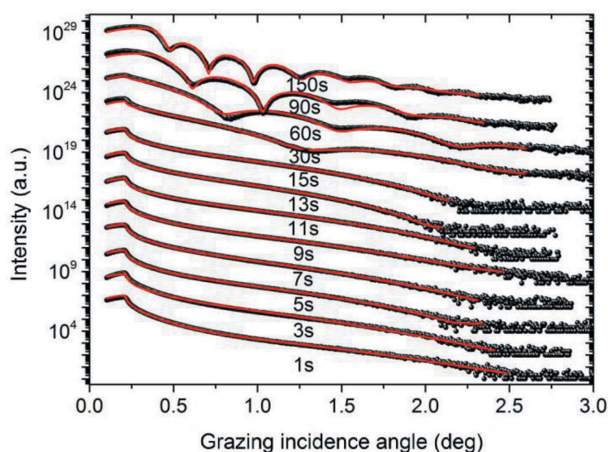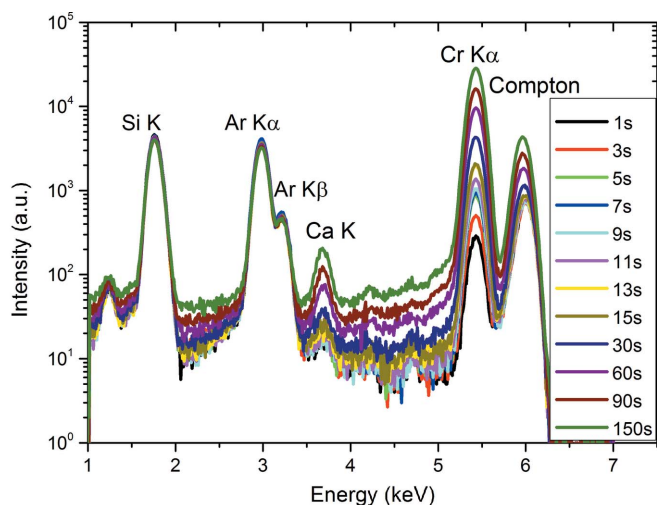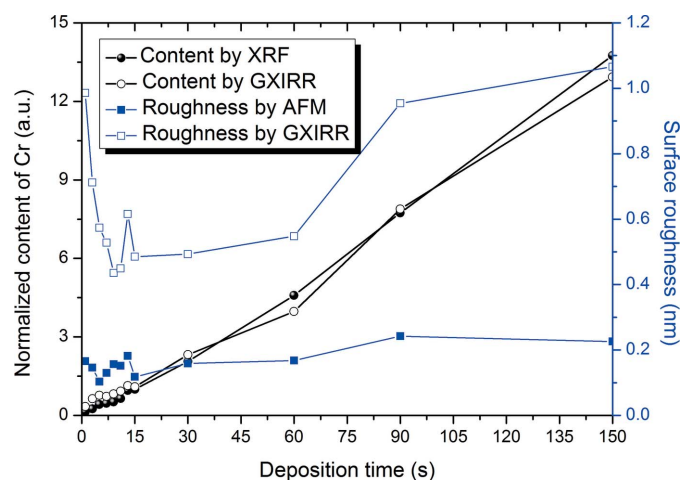

Figure 3
Comparison of the content of Cr in different Cr layers (S1–S12) between XRF (solid circles) and GXIRR (open circles), and the surface roughness between AFM (solid squares) and GXIRR (open squares).

Table 2
Structural parameters of Cr/C and Cr/Sc multilayers.

C (Sc) is the simplified representation of C or Sc in the corresponding Cr-based multilayers.

	d_{Cr} (nm)	$d_{C(Sc)}$ (nm)	$\sigma_{C(Sc)\text{-on-}Cr}$ bottom (nm)	$\sigma_{Cr\text{-on-}C(Sc)}$ bottom (nm)	ρ_{Cr} (% bulk)	$\rho_{C(Sc)}$ (% bulk)	h ($\times 10^{-3}$)
Cr/C (S13, $N = 40$; S14–S16, $N = 20$)							
S13	1.1 ± 0.1	1.5 ± 0.0	0.4 ± 0.1	0.3 ± 0.1	93.8 ± 3.8	125.8 ± 6.1	1.0 ± 0.3
S14	2.6 ± 0.1	2.4 ± 0.1	0.4 ± 0.1	0.3 ± 0.1	86.3 ± 5.1	123.5 ± 8.1	2.0 ± 0.4
S15	4.0 ± 0.0	3.9 ± 0.1	0.3 ± 0.1	0.6 ± 0.1	100.0 ± 4.4	80.5 ± 7.1	5.1 ± 0.5
S16	6.9 ± 0.1	8.3 ± 0.1	0.3 ± 0.1	0.5 ± 0.1	100.0 ± 5.0	86.4 ± 7.0	2.8 ± 0.3
S13 annealed	1.1 ± 0.1	1.4 ± 0.2	1.1 ± 0.2	0.5 ± 0.2	99.8 ± 9.9	129.2 ± 11.5	1.5 ± 0.6
S16 annealed	7.7 ± 0.3	7.7 ± 0.3	1.1 ± 0.2	0.7 ± 0.2	98.9 ± 8.4	124.1 ± 13.0	0.4 ± 0.2
Cr/Sc (S17, $N = 40$; S18–S20, $N = 20$)							
S17	1.4 ± 0.0	1.3 ± 0.0	0.4 ± 0.1	0.8 ± 0.1	90.2 ± 4.3	101.1 ± 7.2	3.0 ± 0.3
S18	2.3 ± 0.1	2.8 ± 0.1	0.3 ± 0.1	0.7 ± 0.1	93.9 ± 5.4	91.0 ± 10.0	3.6 ± 0.4
S19	3.5 ± 0.0	3.9 ± 0.1	0.2 ± 0.1	0.6 ± 0.1	87.7 ± 8.1	94.0 ± 7.4	5.0 ± 0.6
S20	6.9 ± 0.1	7.2 ± 0.1	0.2 ± 0.1	0.6 ± 0.1	100.0 ± 5.3	104.1 ± 7.3	3.7 ± 0.4
S17 annealed	1.4 ± 0.1	1.4 ± 0.1	1.1 ± 0.2	0.6 ± 0.2	99.3 ± 10.3	134.2 ± 14.4	3.8 ± 0.4
S20 annealed	7.3 ± 0.1	7.3 ± 0.1	1.0 ± 0.2'	0.9 ± 0.2	99.0 ± 9.9	128.9 ± 12.8	0.5 ± 0.5

interface from the substrate, D is the periodic thickness and parameter h is the roughness growth rate. The total-reflection regions of the measured curves decay and splitting Bragg peaks occur for four annealed samples due to surface oxidation. The fitted curves do not include the total-reflection regions in order to obtain accurate information about the interior layers. Part of the measured and fitted reflectivity curves can be seen in Fig. 4 and the structural parameters are shown in Table 2. The results reveal that the densities of the Cr layers in multilayers are obviously larger than those of Cr mono-layers with similar thickness levels. Even if an individual Cr layer in each period is ~1 nm, the density is close to 90% of the bulk density. As we know, owing to interlayer diffusion the densities of the two materials influence each other. If heavy-material atoms diffuse into light material and are regarded as
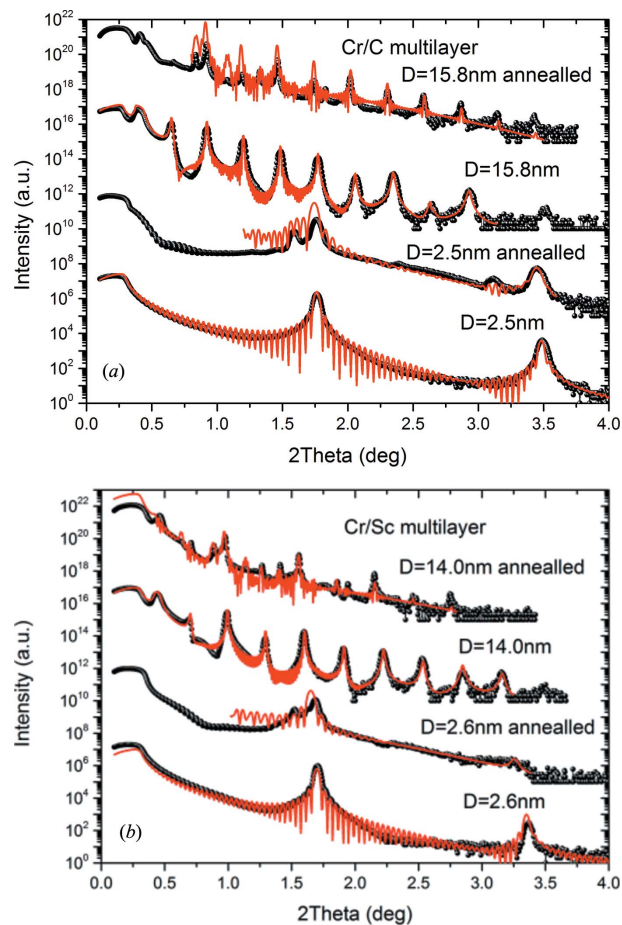
normal because X-rays are sensitive to the relatively low spatial frequency (Kozhevnikov *et al.*, 1999), and the roughness is defined as satisfying a roughness factor (Stoev & Sakurai, 1997) and not just a real surface morphology like AFM. At the initial layer growth, it is found that the surface roughness is large and then gradually decreases after several seconds. In the following seconds, the surface roughness keeps oscillating and has a sudden increase at $t = 13$ s. The oscillating roughness and sudden increase were attributed to measurement errors and a deposition error for layer S7. The roughness gradually increases as the layer thickness increases until the layer thickness is greater than 2 nm. The density also has a similar tendency. In the initial growth, the density is 83% of the bulk density but quickly decreases to ~50%–60% and slowly increases as the layer thickness increases. It is worth noting that at initial growth the fitted layer thickness is smaller than the surface roughness. In this case, the layer did not possess stable density and existed as a non-equilibrium atomic accumulation with a statistical gradient density. Upon further deposition, the layer begins to form a stable layer state and gradually becomes denser. One possible reason for the larger density at the initial growth is that unstable Cr atoms bond easily with a small quantity of O or N atoms. Owing to the small and gradient content of O and N at the surface, an additional layer, *i.e.* $Cr_xO_yN_{1-x-y}$, was not introduced into the fitting model. Until the layer thickness is beyond 9 nm, the Cr layer is close to that of bulk Cr. The lateral correlation length is 349 nm for S1 and decreases to the range ~210–300 nm until the layer thickness increases to 6 nm. When the Cr layers are close to the bulk material, the lateral correlation length remains constant at ~162 nm.

A series of Cr/C (S13–S16) and Cr/Sc (S17–S20) multilayers with different periodic thicknesses were deposited to investigate the characteristics of Cr thin films combined with other materials. The basic structural parameters were determined by GIXRR as well. The interfacial widths from layer to layer are assumed to satisfy the law of structure growth, $\sigma_j^2 = \sigma_{j-1}^2 + hD$ (Pleshanov, 2004), where σ_j is the interfacial width at the jth

Figure 4
GIXRR curves (black points) and their fits (red lines) of (*a*) Cr/C multilayers (S13 and S16) and (*b*) Cr/Sc multilayers (S17 and S20).

part of the light material, it is possible to produce the phenomenon of a larger density of the light material than the bulk value. The atomic numbers of Cr and Sc are close such that their densities remain relatively stable at room temperature. The densities of C layers in thin Cr/C multilayers (S13 and S14) are larger than that of graphite C due to the above-mentioned diffusion phenomenon but decrease as the periodic thickness increases (as in S15 and S16), probably because interfacial diffusion becomes weak and the elementary thin film plays a dominant role. After annealing, the density of the lighter material (C and Sc) in all samples increases significantly. This characteristic results from the interfacial diffusion, which can be validated by the changes of interfacial widths. The interfacial widths increase significantly but the average roughness growth rate h increases slowly or even decreases in S16 and S20. Considering that the interfacial width includes interfacial roughness and interfacial diffusion, the interfacial diffusion increase definitely plays a more important role. Comparing two kinds of multilayers, the Cr-on-Sc interlayer is about 23 times thicker than the Sc-on-Cr interlayer in Cr/Sc multilayers, and Cr-on-C and C-on-Cr interlayers are relatively similar. Cr/C and Cr/Sc multilayers both have clear Bragg peaks after $2\theta = 3.5°$, but after annealing to $600°C$ the Bragg peaks after $2\theta = 3.0°$ for Cr/Sc multilayers can barely be identified. The C(Sc)-on-Cr interlayers broaden remarkably since Cr atoms begin to diffuse to upper adjacent layers at high temperature.

Scaling theory is often used to predict non-equilibrium thin film growth including spatial and temporal scaling behaviors. Some models such as the Kardar–Parisi–Zhang (KPZ) equation (Kardar *et al.*, 1986) were used to describe relaxation of surface and random fluctuations. For models within the KPZ class, the main properties of the surface height profiles can be characterized by the Family–Vicsek scaling relation (Family & Vicsek, 1985) of the roughness: $\sigma(L,t) \simeq L^\alpha f(t/L^z)$, where t is the deposition time, L is the length scale over the measured range, and α, β and $z = \alpha/\beta$ are the roughness, growth and dynamic exponents, respectively. When the deposition time is short, the dependence of surface roughness is characterized by the growth exponent: $\sigma_{r.m.s.} = t^\beta$. The value of β normally indicates different growth modes (Lita & Sanchez, 1999). Fig. 5 shows the surface roughness of Cr monolayers as a function of layer thickness on a double-logarithmic scale. Based on the analysis of GIXRR, three regions can be used to describe the growth process, with the growth exponents $\beta_1 = -0.36 \pm 0.03$, $\beta_2 = 0.11 \pm 0.02$ and $\beta_3 = 0.22$. In the first region the growth exponent is a negative value. The layers are discontinuous or at least have a discontinuous-to-continuous transition status. It is worth noting that the density fitted by GIXRR does not satisfy a monotonic decrease, but the roughness decreases rapidly. This process can be described as the transition process from the island growth mode (Volmer–Weber mode) (Volmer & Weber, 1926) to the layer plus island growth mode (Stranski–Krastanov mode) (Mo *et al.*, 1990). The large-size island structures with a high density of Cr nuclei begin to aggregate and tend to form a layer structure (Rosenfeld *et al.*, 1993). The second region has a very low growth exponent of
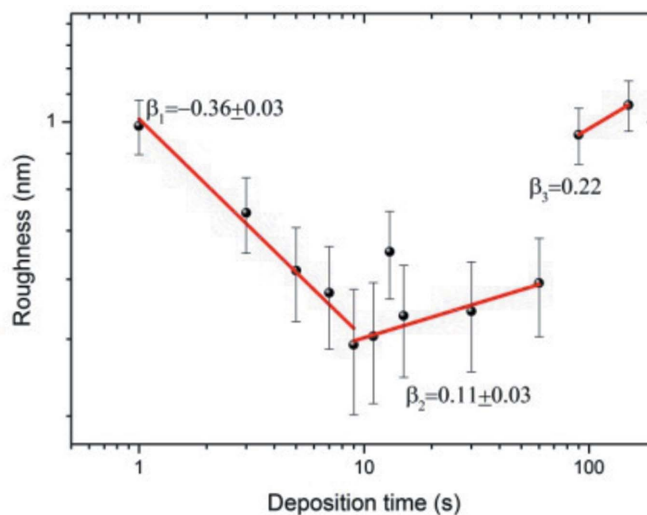

Figure 5
Roughness of Cr layers as a function of layer thickness.

0.11 ± 0.02, which is attributed to the dominant effect of surface diffusion (Yu *et al.*, 2008). Considering the deposition technology of low Ar pressure and $T/T_m < 0.3$ where T is the deposition temperature on the substrate and T_m the melting temperature of Cr, the microstructure of the Cr layer presents a columnar structure with void streaks, which are attributed to nucleation and coalescence (Thornton, 1986). In this region, the surface adhesive force is significantly stronger than the adatom cohesive force. Sufficiently high surface mobility drives atoms to fill these voids and gradually form a more continuous and denser layer. The third region has a growth exponent of 0.22, which is in the range of most previous reports for similar systems (Wang *et al.*, 2003; Freitag & Clemens, 2001). In this process, the bulk of the layer is very close to crystalline Cr with larger grain size and fewer void streaks.

In multilayer cases, the obvious improvement compared with monolayers is the density of the layers. In addition to the fact that interfacial diffusion fills voids in layers, the growth mode also changes with the different deposition environments. Most metal deposited on another metal has been reported to tend to a layer-growth mode (Frank–van der Merwe mode) rather than to the Stranski–Krastanov mode when deposited on semiconductor material (Lüth, 2010). C has less surface free energy compared with Sc, which enables a new layer to easily form while being deposited on the Cr layer to improve interfacial roughness and layer density.

3.2. Crystallization and atomic environment characterizations

Structure and morphology characterization is not sufficient for a comprehensive understanding of the regulation of film growth and interface characteristics. Therefore, studies on crystallization, chemical interaction and even atomic transitions become meaningful and necessary.

Fig. 6 presents GIXRD spectra for multilayers (S13–S20), and Cr and Sc monolayers (S12 and S21) were also measured
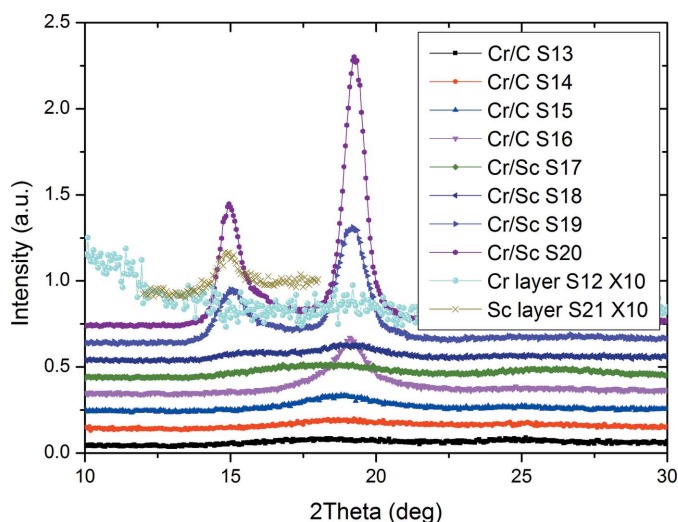
Figure 6
GIXRD spectra of Cr/C and Cr/Sc multilayers; those of Cr and Sc layers are also shown for comparison.

for comparison. The pronounced peaks at $2\theta = \sim 19°$ and $\sim 15°$ are assigned, respectively, to cubic Cr(110) and hexagonal close-packed α-Sc(101), which matches the results of previous studies (Ghafoor *et al.*, 2008; http://database.iem.ac.ru/mincryst/s_chem.php?present=Sc&absent=), and agrees with the report on their preferred orientation (Gorelik *et al.*, 2004). All Cr(110) diffraction peaks tend to move towards higher angle as a function of periodic thickness, which may result from increasing internal stress. Concerning multilayers with short period, only broadened peaks corresponding to amorphous layers can be observed. Sharp diffraction peaks occur in S16, S19 and S20, indicating that a Cr layer only 3.5 nm thick transforms to crystallization in Cr/Sc multilayers, whereas in Cr/C multilayers the Cr layer produces strong crystallinity until the thickness is beyond 6 nm. Based on the Scherrer equation (Patterson, 1939), the particle size of Cr(110) crystals can be estimated. For the samples S15, S16, S19 and S20, the particle sizes are 1.2, 2.2, 3.2 and 4.4 nm, respectively.

As can be seen in both Figs. 7(*a*) and 7(*b*), when annealed beyond 400°C, a peak at $2\theta = \sim 16.5°$ occurs and gradually becomes strong whereas the sharp Cr(110) peaks become weak. This peak matches Cr_2O_3(110) (Gorelik *et al.*, 2004). The situation is different for Cr/Sc multilayers. When the annealing temperature is greater than 400°C, except for when the Cr_2O_3(110) peak is found, a stronger peak occurs at $2\theta = \sim 17.6°$. This peak is not assigned to any oxidation state of Cr and Sc, and previous studies showed no intermediate phase in the Cr–Sc system, as with other Cr–rare-earth-metal systems (Venkatraman & Neumann, 1985). It is suggested that this peak is assigned to generate the cubic β-Sc(200) phase under high-temperature conditions (Gorelik *et al.*, 2004; Venkatraman & Neumann, 1985; http://database.iem.ac.ru/mincryst/s_chem.php?present=Sc&absent=).

The XANES measurements were performed in fluorescence mode. Parts of the Cr *K*-edge XANES spectra of the Cr monolayers and Cr foil are shown in Fig. 8. Pre-edge features become stronger as the layer thickness increases and move

from 5.994 to 5.992 keV. These features result from the 1*s*-to-3*d* transition to an unoccupied electron state. A low symmetry of the ligand to produce hybridization of 3*d* and 4*p* orbitals partially allows dipole forbidden transitions or quadrupolar
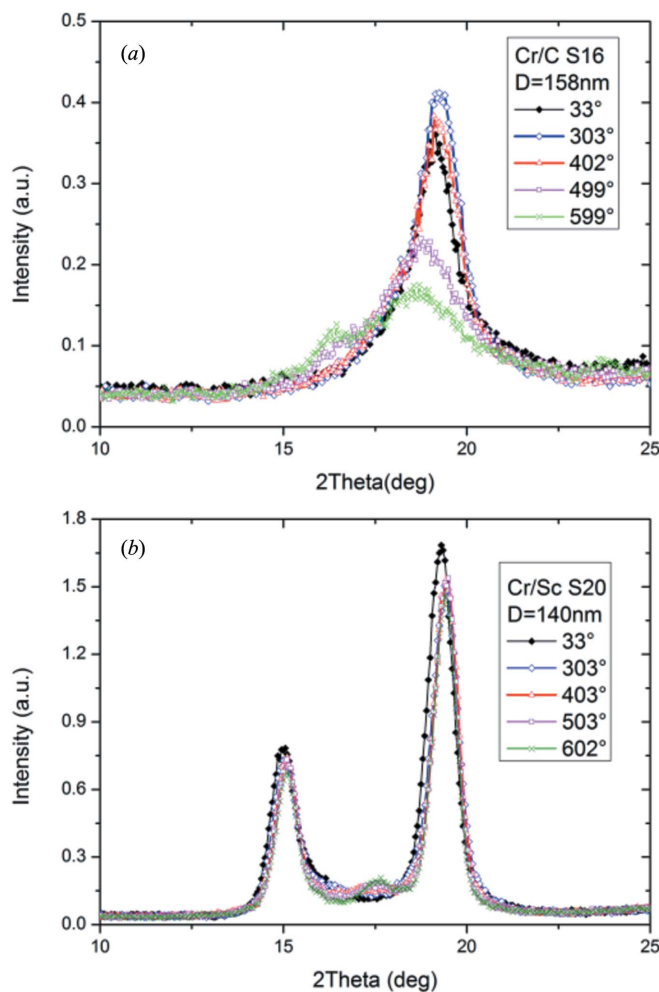

Figure 7
GIXRD curves of (*a*) Cr/C (S16) and (*b*) Cr/Sc (S20) multilayers as annealing temperature increases.
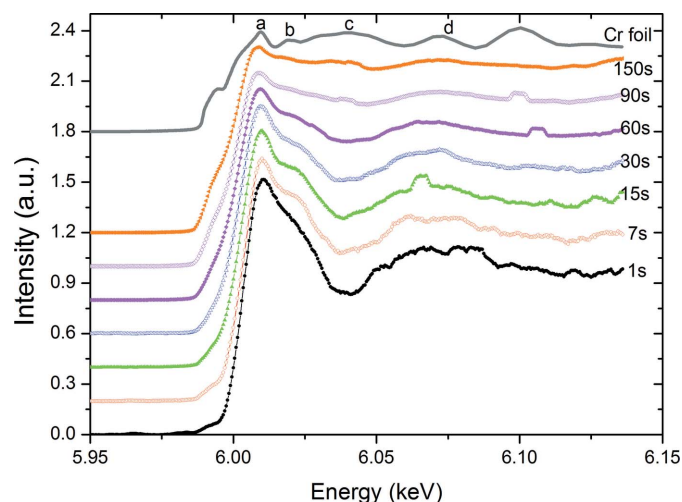

Figure 8
Comparison of the experimental Cr *K*-edge XANES spectra for part of Cr monolayers and Cr foil.

transitions (Pong *et al.*, 1999). The white-line main peak (peak *a*) from the 1*s*-to-4*p* transition exhibits a shift from 6.011 to 6.007 keV and obviously becomes weak as the layer thickness increases. The edge shift relates to the binding energy of the inner-shell electrons and reveals that the partial oxidation state transfers to elemental Cr. For thinner layers, broken chemical bonds at the surface play a dominant role and easily trap O and N atoms in the air. This also explains the phenomenon that a larger density of the Cr monolayer is determined by GIXRR at initial growth. A sharp white-line peak normally reveals better ligand symmetry, probably from the octahedral structure of Cr_2O_3 (Tromp *et al.*, 2007). The most notable difference between different Cr monolayers is that peak *c* (~6.039 keV) occurs when the layer thickness is larger than 9 nm. Related to the GIXRR results, a Cr layer thicker than 9 nm has a density close to that of crystal Cr bulk and tends to produce similar ligand surroundings compared with Cr foil. The XANES spectra of Cr/C and Cr/Sc multilayers with the shortest and thickest periods are compared in Fig. 9. Different from the Cr monolayers, pre-edge peaks can be found at ~5.964 keV for all multilayer samples, which are especially strong in the Cr/Sc multilayers, which was not reported by previous studies. The pre-edge oscillation at ~5.99 keV is similar to that in Cr foil. The features of a main peak and after the peak are very different between Cr/C and Cr/Sc multilayers. Cr/C multilayers are similar to Cr monolayers whereas Cr/Sc multilayers are very similar to Cr foil. The broader maxima *d* (~6.072 keV) and *e* (~6.100 keV) are clearer in Cr/Sc multilayers and high temperatures make these maxima stronger. These features originate from continuous 'inner well' states (Dehmer, 1972) that result from a potential barrier formed by the electronegative ligand surroundings. Cr and Sc are both transition metals, so they easily gain and lose electrons. As the crystalline state increases and the metal bond plays a dominant role, Cr and Sc present strong electronegative ligand surroundings. The annealing process produces more serious diffusio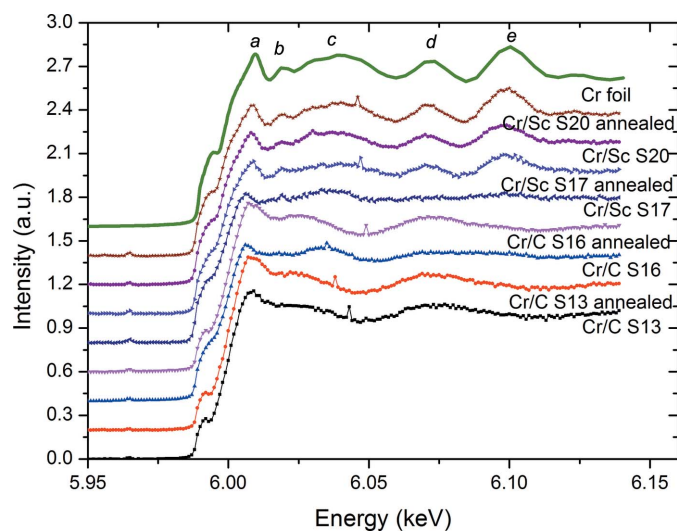n and increases the opportunity for a 1*s*-to-'inner well' transition. Other Cr/metal multilayers are expected to have similar ligand surroundings as Cr/Sc multilayers. A similar phenomenon was not found in Cr/C multilayer spectra. The C layers block the formation of a large number of electronegative ligand surroundings. Ionic bonding may be more pronounced like the local structure of Cr oxide in monolayers.

4. Conclusions

In this paper, various Cr monolayers and Cr/C and Cr/Sc multilayers with different layer thicknesses deposited by magnetron sputtering techniques are systematically studied in terms of their structure, morphology, atomic environment, *etc*. GIXRR and GIXRD studies of Cr monolayers reveal that there are three obvious growth stages scaled by different growth exponents, *i.e.* island aggregation, layer densification and crystallization. Cr-based multilayers exhibit a denser structure due to interfacial diffusion and layer growth mode. Cr/Sc multilayers have a larger interfacial roughness than Cr/C multilayers and asymmetrical interfacial widths. It is easier for Cr layers to crystallize in Cr/Sc multilayers than in Cr/C multilayers. After annealing, chromium oxides and β-Sc phases occur in multilayers and Cr/Sc is more unstable at high temperature. Cr/Sc multilayers present strong electronegative ligand surroundings and similar ligand status as Cr foil, whereas Cr/C multilayers are similar to Cr monolayers. The experimental results enable us to symmetrically understand the growth characteristics and the interface evolutions of Cr monolayers and Cr-based multilayers. In the future, interfacial diffusion and void defects in multilayers with ultra-short period should be studied in order to further improve reflectivity in the water-window region and focusing resolution based on multilayer optics in the synchrotron field.

Figure 9
Comparison of the experimental Cr *K*-edge XANES spectra for part of Cr/C and Cr/Sc multilayers and Cr foil.

References

Alnaimi, R., Wang, H., Zhang, Z., Yang, X. & Wen, M. (2016). *Optik*, **127**, 588–592.

Andreev, S. S., Bibishkin, M. S., Chkhalo, N. I., Kluenkov, E. B., Prokhorov, K. A., Salashchenko, N. N., Zorina, M. V., Schafers, F. & Shmaenok, L. A. (2003). *J. Synchrotron Rad.* **10**, 358–360.

Birch, S. J., Eriksson, F., Johansson, G. A. & Hertz, H. M. (2003). *Vacuum*, **68**, 275–282.

Burcklen, C., Soufli, R., Dennetiere, D., Polack, F., Capitanio, B., Gullikson, E., Meltchakov, E., Thomasset, M., Jérome, A., de Rossi, S. & Delmotte, F. (2016). *J. Appl. Phys.* **119**, 2141–2165.

research papers

Chkhalo, N., Churin, S. A., Pestov, A. E., Salashchenko, N. N., Vainer, Y. A. & Zorina, M. V. (2014). *Opt. Express*, **22**, 20094–20106.

Dehmer, J. L. (1972). *J. Chem. Phys.* **56**, 4496–4504.

Deng, S., Qi, H., Yi, K., Fan, Z. & Shao, J. (2009). *Appl. Surf. Sci.* **255**, 7434–7438.

Family, F. & Vicsek, T. (1985). *J. Phys. A*, **18**, L75–L81.

Freitag, J. M. & Clemens, B. M. (2001). *J. Appl. Phys.* **89**, 1101–1107.

Gadioli, G. Z., Rouxinol, F. P., Gelamo, R. V., Cardoso, L. P., Gama, S. & de Moraes, M. A. B. (2013). *Thin Solid Films*, **545**, 496–502.

Ghafoor, N., Eriksson, F., Aquila, A., Gullikson, E., Schäfers, F., Greczynski, G. & Birch, J. (2017). *Opt. Express*, **25**, 18274–18287.

Ghafoor, N., Eriksson, F., Gullikson, E., Hultman, L. & Birch, J. (2008). *Appl. Phys. Lett.* **92**, 091913.

Gorelik, T., Kaiser, U., Kuhlmann, T., Yulin, S. & Richter, W. (2004). *Appl. Surf. Sci.* **230**, 1–7.

Guggenmos, A., Rauhut, R., Hofstetter, M., Hertrich, S., Nickel, B., Schmidt, J., Gullikson, E. M., Seibald, M., Schnick, W. & Kleineberg, U. (2013). *Opt. Express*, **21**, 21728–21740.

Gullikson, E. M., Salmassi, F., Aguila, A. L. & Dollar, F. (2006). *Proceedings of the 8th international Conference on the Physics of X-ray Multilayer Structures*, 12–16 March, 2006, Sapporo, Japan.

Haase, A., Bajt, S., Hönicke, P., Soltwisch, V. & Scholze, F. (2016). *J. Appl. Cryst.* **49**, 2161–2171.

Hatano, T., Ejima, T. & Tsuru, T. (2017). *J. Electron Spectrosc. Relat. Phenom.* **220**, 14–16.

Hignette, O., Cloetens, P., Morawe, C., Borel, C., Ludwig, W., Bernard, P., Rommeveaux, A. & Bohic, S. (2007). *AIP Conf. Proc.* **879**, 792–795.

Huang, Q., Fei, J., Liu, Y., Li, P., Wen, M., Xie, C., Jonnard, P., Giglia, A., Zhang, Z., Wang, K. & Wang, Z. (2016). *Opt. Lett.* **41**, 701–704.

Jergel, M., Majkova, E., Borel, C., Morawe, C. & Matko, I. (2008). *Modern Developments in X-ray and Neutron Optics*, Vol. 137 of *Springer Series in Optical Science*, pp. 389–406. Springer.

Jiang, H., Michette, A., Pfauntsch, S., Wang, Z., Zhu, J. & Li, D. (2011). *Opt. Express*, **19**, 11815–11824.

Kardar, M., Parisi, G. & Zhang, Y. (1986). *Phys. Rev. Lett.* **56**, 889–892.

Kozhevnikov, I. V., Asadchikov, V. E., Duparre, A., Gilev, O. N., Havronin, N. A., Krivonosov, Y. S., Ostashev, V. I. & Steinert, J. (1999). *Proc. SPIE*, **3739**, 348–354.

Lita, A. & Sanchez, J. (1999). *J. Appl. Phys.* **85**, 876–882.

Lüth, H. (2010). *Solid Surfaces, Interfaces and Thin Films*, pp. 100–103. Springer.

Majkova, E., Chushkin, Y., Jergel, M., Luby, S., Holy, V., Matko, I., Chenevier, B., Toth, L., Hatano, T. & Yamamoto, M. (2006). *Thin Solid Films*, **497**, 115–120.

Miyanaga, T., Takasagi, K., Ohba, T., Takahiro, A. & Teiko, O. (2014). *J. Phys. Conf. Ser.* **502**, 012032.

Mo, Y., Savage, D. E., Swartzentruber, B. S. & Lagally, M. G. (1990). *Phys. Rev. Lett.* **65**, 1020–1023.

Niibe, M., Mukai, M., Kimura, H. & Shoji, Y. (2004). *AIP Conf. Proc.* **705**, 243–246.

Parratt, L. G. (1954). *Phys. Rev.* **95**, 359–369.

Patterson, A. (1939). *Phys. Rev.* **56**, 978–982.

Pleshanov, N. K. (2004). *Nucl. Instrum. Methods Phys. Res. A*, **524**, 273–286.

Pong, W. F., Liou, Y. C., Chang, K. H., Tsai, M.-H., Hsieh, H. H., Chang, Y. K., Tseng, P. K., Lee, J. F., Liou, Y. & Huang, J. C. A. (1999). *J. Synchrotron Rad.* **6**, 746–748.

Ramakrishna, B. L., Lee, C. H., Cheng, Y. & Stearns, M. B. (1987). *J. Appl. Phys.* **61**, 4290–4292.

Rosenfeld, G., Servaty, R., Teichert, C., Poelsema, B. & Comsa, G. (1993). *Phys. Rev. Lett.* **71**, 895–898.

Stoev, K. & Sakurai, K. (1997). *Rigaku J.* **14**, 22–37.

Stollberg, H., Yulin, S., Takman, P. A. C. & Hertz, H. M. (2006). *Rev. Sci. Instrum.* **77**, 23101.

Thornton, J. A. (1986). *J. Vac. Sci. Technol. A*, **4**, 3059–3065.

Tromp, M., Moulin, J., Reid, G. & Evans, J. (2007). *AIP Conf. Proc.* **882**, 699–701.

Tu, Y., Zhu, J., Li, H., Jonnard, P., Le Guen, K., André, J.-M., Chen, H. & Wang, Z. (2014). *Appl. Surf. Sci.* **313**, 341–345.

Venkatraman, M. & Neumann, J. (1985). *Bull. Alloy Phase Diagrams*, **6**, 422–423.

Volmer, M. & Weber, A. (1926). *Z. Phys. Chem.* **119**, 277–301.

Wang, X., Zheng, W. T., Gao, L. J., Wei, L., Guo, W., Bai, Y. B., Fei, W. D., Meng, S. H., He, X. D. & Han, J. C. (2003). *J. Vac. Sci. Technol. A*, **21**, 983–987.

Wen, M., Jiang, L., Zhang, Z., Huang, Q., Wang, Z., She, R., Feng, H. & Wang, H. (2015). *Thin Solid Films*, **592**, 262–265.

Yan, H., Maser, J., Macrander, A., Shen, Q., Vogt, S., Stephenson, B. & Kang, H. C. (2007). *Phys. Rev. B*, **76**, 115438.

Yang, T., Wen, W., Yin, G., Li, X., Gao, M., Gu, Y., Li, L., Liu, Y., Lin, H., Zhang, X., Zhao, B., Liu, T., Yang, Y., Li, Z., Zhou, X. & Gao, X. (2015). *Nucl. Sci. Tech.* **26**, 020101.

Yu, L., Xu, J., Dong, S. & Kojima, I. (2008). *Thin Solid Films*, **516**, 1781–1787.

Zhang, L., Yan, S., Jiang, S., Yang, K., Wang, H., He, S., Liang, D., Zhang, L., He, Y., Lan, X., Mao, C., Wang, J., Jiang, H., Zheng, Y., Dong, Z., Zeng, L. & Li, A. (2015). *Nucl. Sci. Tech.* **26**, 060101.